Enceladus' and Dione's floating ice shells supported by minimum stress isostasy

Mikael Beuthe[1], Attilio Rivoldini[1], Antony Trinh[1]

mikael.beuthe@observatory.be

M. Beuthe

[1]Royal Observatory of Belgium, Brussels, Belgium

This article has been accepted for publication and undergone full peer review but has not been through the copyediting, typesetting, pagination and proofreading process, which may lead to differences between this version and the Version of Record. Please cite this article as doi: 10.1002/2016GL070650

©2016 American Geophysical Union. All Rights Reserved.

Abstract. Enceladus' gravity and shape have been explained in terms of a thick isostatic ice shell floating on a global ocean, in contradiction of the thin shell implied by librations. Here we propose a new isostatic model minimizing crustal deviatoric stress, and demonstrate that gravity and shape data predict a 38 ± 4 km-thick ocean beneath a 23 ± 4 km-thick shell agreeing with – but independent from – libration data. Isostatic and tidal stresses are comparable in magnitude. South polar crust is only 7 ± 4 km thick, facilitating the opening of water conduits and enhancing tidal dissipation through stress concentration. Enceladus' resonant companion, Dione, is in a similar state of minimum stress isostasy. Its gravity and shape can be explained in terms of a 99 ± 23 km-thick isostatic shell overlying a 65 ± 30 km-thick global ocean, thus providing the first clear evidence for a present-day ocean within Dione.

Key points:

- New isostatic model minimizing crustal stresses
- Enceladus' gravity-shape data predict a 23 km-thick ice shell in agreement with librations
- Subsurface ocean in Dione under a 100 km-thick ice shell

©2016 American Geophysical Union. All Rights Reserved.

1. Introduction

Saturn's moon Enceladus is celebrated for its huge south polar fractures venting jets of water vapour and ice particles [*Porco et al.*, 2006] while its neighbour Dione is more discreet, though essential in maintaining Enceladus' eccentricity through a 2:1 orbital resonance. The composition of Enceladus' plume shows that it originates in a subsurface ocean in contact with a silicate core [*Postberg et al.*, 2011; *Hsu et al.*, 2015], but a more detailed picture of the interior must be based on geodesy. Inferences about the internal structure of Enceladus and Dione were first based on their long-wavelength shape [*Thomas et al.*, 2007; *Nimmo et al.*, 2011] and gravity field [*Iess et al.*, 2014; *Hemingway et al.*, 2016]. These data reveal the presence of a hydrated silicate core with a radius of about three-fourths of the surface radius, but the crust-ocean partition of the outer H_2O mantle has remained controversial. The recent measurement of Enceladus' librations [*Thomas et al.*, 2016; *Nadezhdina et al.*, 2016] demonstrates that the crust is a thin ice shell floating on a global ocean.

For both satellites, the task of building interior models compatible with the gravity and shape data is complicated by strong deviations from hydrostatic equilibrium. For synchronously rotating satellites, nonhydrostatic deviations can be estimated either from the gravity ratio J_2/C_{22} or from the analog ratio for the shape (Text S1). If the satellite is hydrostatic, these shape and gravity ratios are both equal to 10/3 to first order in the flattening [*Zharkov et al.*, 1985]. Using the shape and gravity data of Cassini and taking into account second-order corrections, one concludes that the observed shape and gravity ratios of Enceladus deviate from hydrostaticity by thirty and ten percent, respec-

©2016 American Geophysical Union. All Rights Reserved.

tively, whereas the corresponding deviations for Dione are twice as large (Text S1). Such differences between the nonhydrostatic components of shape and gravity are indicative of isostasy, in which surface topography is mechanically supported and gravitationally compensated by a subsurface mass anomaly in such a way that below a certain depth, called the compensation depth, pressure is everywhere hydrostatic [*Lambeck*, 1980, 1988]. Enceladus' degree-three zonal gravity harmonic (J_3) also points to isostasy: it is fully nonhydrostatic and nonzero within its 3σ error interval, but only a third of what is expected from the corresponding shape harmonic. Degree-three compensation is attributed to isostatic support of the south polar depression [*Iess et al.*, 2014].

In this paper, we reexamine the two main aspects of the method of *Iess et al.* [2014] and *McKinnon* [2015]: the second-order figure of equilibrium and the isostatic compensation model. Our computation of the figure of equilibrium is more rigorous but does not make a significant numerical difference. By contrast, our new theory of isostasy has important implications for the structure of the H_2O mantle. We put our conclusions on a firm footing by doing a Bayesian inversion of the gravity data taking into account the uncertainties on the shape and gravity.

2. The Problem with Classical Isostasy

Isostasy can occur either through crustal density variations (Pratt) or through variations in crustal thickness (Airy). For Pratt isostasy, the only plausible scenario involves porosity variations close to the surface, but compensation is too high [*McKinnon*, 2015]. With Airy isostasy, Enceladus' ice shell was initially estimated to be on average 30 to 40 km thick [*Iess et al.*, 2014], but this value was revised to 50 km due to second-order tidal-rotational effects [*McKinnon*, 2015]. A thick shell is hardly compatible with the south polar activity,

©2016 American Geophysical Union. All Rights Reserved.

raises the issue of shell-core contact at the equator precluding isostasy, and does not match degree-three compensation [*McKinnon*, 2015]. Furthermore, the result conflicts with libration models predicting that the shell is half as thick [*Thomas et al.*, 2016; *Van Hoolst et al.*, 2016]. Compared to Enceladus, Dione's case is even more serious because the 180 km-thick ice shell implied by Airy isostasy does not fit into the 150 km-thick H_2O mantle [*Hemingway et al.*, 2016] (see also Fig. 1). Although a solution is possible within 1σ uncertainties, it entails that Dione's shape deviates even more from hydrostaticity.

The easy way out is to suppose that an elastic lithosphere partly supports the load (flexural isostasy) so that the subsurface mass anomaly can be smaller and located closer to the surface. Flexural support of long-wavelength loads, however, generates stresses that are not only larger than the tensional strength of intact ice (1 to 2 MPa [*Schulson and Duval*, 2009]) but also much above the Coulomb failure criterion for a pervasively cracked thin lithosphere [*McKinnon*, 2013]. *Cadek et al.* [2016] nevertheless argued for partial support of Enceladus' topography by a thin lithosphere, without addressing the question of lithospheric failure. Besides, they overestimate the elastic thickness required for top loading by a factor of ten [*Turcotte et al.*, 1981; *McGovern et al.*, 2002; *Kalousová et al.*, 2012]. We give a detailed rebuttal of *Cadek et al.* [2016] in the Supporting Information (Text S7).

Classical Airy (or Pratt) isostasy is plagued by ambiguities about the isostatic prescription, i.e. the constraint relating the subsurface mass anomaly to the surface load [*Vening Meinesz*, 1946]. At the longest wavelengths, various isostatic prescriptions lead to geoid anomalies differing by more than a factor of two [*Dahlen*, 1982]. This question has never been settled because of the complexity of large-scale isostasy on Earth: thermal (Pratt)

©2016 American Geophysical Union. All Rights Reserved.

and Airy isostasy are dominant in oceanic and continental crusts, respectively, while the long-wavelength geoid is explained by mantle convection. In planetology, isostasy invariably resorts to the equal-mass prescription applied to conical columns [*Lambeck*, 1988]. This prescription however neither takes into account horizontal stresses nor geoid perturbations due to the loads themselves. Here we consider instead (following *Jeffreys* [1970] and *Dahlen* [1982]) that the only physically meaningful isostatic prescription consists in minimizing crustal deviatoric stress in a self-consistent elastic-gravitational theory.

3. Methods

3.1. Hydrostatic-Isostatic Decomposition

Before explaining the three methods particular to this paper, we recall the principle of the hydrostatic-isostatic decomposition. Let H_{nm} and C_{nm} denote the cosine real harmonic coefficients of degree n and order m of the shape and nondimensional gravity potential, respectively. Following *Iess et al.* [2014], we split the harmonic components into hydrostatic and isostatic (nonhydrostatic) components:

$$H_{nm} = H^h_{nm} + H^{iso}_{nm} \,. \tag{1}$$

$$C_{nm} = C^h_{nm} + C^{iso}_{nm} \,, \tag{2}$$

The hydrostatic components with $n = 2$ and $m = (0, 2)$ are determined by computing the figure of equilibrium (the other hydrostatic components vanish). At each harmonic degree n, the isostatic components are related by the isotropic admittance Z_n (or equivalently by the nondimensional compensation factor f_n) characterizing the isostatic model:

$$C^{iso}_{nm} = Z_n \, H^{iso}_{nm} = \frac{3\rho_s}{(2n+1)R\bar{\rho}} \, f_n \, H^{iso}_{nm} \,, \tag{3}$$

where ρ_s is the ice shell density, $\bar{\rho}$ is the bulk density and R is the surface radius.

©2016 American Geophysical Union. All Rights Reserved.

3.2. Figure of Equilibrium

Enceladus' rapid rotation leads to significant deviations from the first order figure of equilibrium. Contrary to *McKinnon* [2015], we do not compute the figure of equilibrium with the method of *Tricarico* [2014], which is based on nested ellipsoids, because an ellipsoidal stratification is forbidden for heterogenous hydrostatic bodies (Hamy-Pizzetti theorem, see *Moritz* [1990]). We work instead with the classical theory of equilibrium figures extended from first order (Clairaut's equation) to second order in the flattening [*Zharkov*, 2004].

Solving the second-order equations for a multilayer body yields complicated expressions for the degree-two shape and gravity coefficients (the latter normalized with respect to the mean radius). These complete solutions to second order are closely approximated by compact formulas depending on the fluid Love numbers k_2^F and $h_2^F = 1 + k_2^F$:

$$\frac{1}{R}\left(H_{20}^h, H_{22}^h\right) = \left(-\frac{5}{6}\left(1+\epsilon_0\right), \frac{1}{4}\left(1+\epsilon_2\right)\right) h_2^F q\,, \tag{4}$$

$$\left(C_{20}^h, C_{22}^h\right) = \left(-\frac{5}{6}\left(1+\delta_0\right), \frac{1}{4}\left(1+\delta_2\right)\right) k_2^F q\,, \tag{5}$$

where $(\epsilon_0, \epsilon_2, \delta_0, \delta_2) = (76/5, 44, 16, 64) h_2^F q/21$ are the second-order corrections and $q = \omega^2 R^3/GM$ is the nondimensional rotational parameter (Table S1). Fluid Love numbers of two- and three-layer bodies are given in *Zharkov* [2004] and *Zharkov and Gudkova* [2010], respectively. We computed C_{2m}^h from H_{2m}^h using the second-order relations between shape and gravity (Eq. (49) of *Zharkov and Gudkova* [2010]). Our formalism for the harmonic coefficients of degree two is equivalent to the one of *Zharkov and Gudkova* [2010], except that their Eqs. (51)-(52) and (57)-(58) are wrong and must be replaced by the two equations above.

©2016 American Geophysical Union. All Rights Reserved.

The error on Eqs. (4)-(5) is similar to the error on the method of *Tricarico* [2014]. It is of third order in the flattening if the satellite is homogeneous. If not, the error is formally of second order, but numerically of third order. Compared to the method of *Tricarico* [2014], Eqs. (4)-(5) are simpler to use and more easily applicable to multilayer bodies. For the Bayesian inversion, we do not use Eqs. (4)-(5) but the complete solutions of the classical approach to second order (i.e. the error is strictly of third order).

3.3. Minimum Stress Isostasy

The principle of minimum stress isostasy is based on the idea that, over time, the crust has reached the state of minimum deviatoric stress compatible with the observed topography through internal deformation, lithospheric failure and viscoelastic relaxation [*Dahlen*, 1981]. The last mechanism depends on the possible viscoelastic processes and the loading timescale. These questions cannot be answered without knowing more about the crust (rheology and thermal state) and about the origin of the putative shell thickness variations. If desired, one can relax the assumption of minimum stress so as to include less bottom loading and more flexural support (flexural isostasy), but the model is not predictive if we don't know the elastic thickness of the lithosphere. Our results will show that such additional parameter is not needed, and we tend to favour the simplest model that can successfully explain the observations. We thus assume here that the crust has reached the state of minimum stress isostasy at the largest scale.

In order to minimize crustal stresses, we need to know the deformations, gravity field perturbations, and stresses due to loads acting on the top and bottom of the crust. In terms of standard geophysical techniques, this means computing the elastic Love numbers of a self-gravitating spherically symmetric body submitted on the one hand to a surface

©2016 American Geophysical Union. All Rights Reserved.

load and, on the other, to an internal load located at the crust-ocean boundary. The two solutions are linearly combined with an arbitrary loading ratio, which is then fixed by minimizing the second invariant of the deviatoric stress tensor. The result takes the form of Eq. (3).

We solve the elastic-gravitational problem with the incompressible propagator matrix method [*Sabadini and Vermeersen*, 2004]. The surface and internal loads are modelled as thin layers with densities (per unit surface) σ^L_{nm} and σ^I_{nm}, respectively. The surface load Love numbers (k^L_n, h^L_n) and the internal load Love numbers (k^I_n, h^I_n) are obtained as boundary values of the full solution. By definition, the perturbation of the gravity potential C^{iso}_{nm} and the radial displacement of the surface u_{nm} read [*Greff-Lefftz et al.*, 2010]

$$\begin{aligned} C^{iso}_{nm} &= \left(1 + k^L_n\right) U^L_{nm} + \left(x^{n+1} + k^I_n\right) U^I_{nm} \,, \\ u_{nm} &= \left(h^L_n \, U^L_{nm} + h^I_n \, U^I_{nm}\right) / g \,, \end{aligned} \tag{6}$$

where $U^L_{nm} = 4\pi G R \sigma^L_{nm}/(2n+1)$ and $U^I_{nm} = 4\pi G R x \sigma^I_{nm}/(2n+1)$ are the loading potentials (g is the surface gravity and $x = 1 - d_s/R$ where d_s is the shell thickness). The former potential depends on the topography through $U^L_{nm} = g\xi_n(H^{iso}_{nm} - u_{nm})$ where $\xi_n = 3\rho_s/((2n+1)\bar{\rho})$, while the latter can initially be written as $U^I_{nm} = \zeta_n U^L_{nm}$, where the *loading ratio* ζ_n is a negative number of order unity to be fixed by the isostatic prescription. The compensation factor follows from Eq. (3):

$$f_n = \frac{1 + k^L_n + \zeta_n \left(x^{n+1} + k^I_n\right)}{1 + \xi_n \left(h^L_n + \zeta_n \, h^I_n\right)} \,. \tag{7}$$

The final step consists in computing the loading ratio with the chosen isostatic prescription. The magnitude of deviatoric stresses can be measured with the second invari-

©2016 American Geophysical Union. All Rights Reserved.

ant of the deviatoric stress tensor $\tau_{\rm II}$ [*Dahlen*, 1982] which is proportional to the shear (or distortional) strain energy density [*Jaeger et al.*, 2007]. For each harmonic degree n, we minimize the total shear energy of the crust $\mathcal{E}_\mu$, which depends quadratically on crustal deformations (Eq. (8.128) of *Dahlen and Tromp* [1999] restricted to the crustal volume). Since crustal deformations are linear combinations of the deformations due to the surface and internal loads, the total shear energy of the crust can be decomposed as $\mathcal{E}_\mu = \mathcal{E}_\mu^{LL} + 2\zeta_n \mathcal{E}_\mu^{LI} + \zeta_n^2 \mathcal{E}_\mu^{II}$ where the terms $(\mathcal{E}_\mu^{LL}, \mathcal{E}_\mu^{LI}, \mathcal{E}_\mu^{II})$ do not depend on ζ_n. Crustal stresses are minimum for the loading ratio $\zeta_n = -\mathcal{E}_\mu^{LI}/\mathcal{E}_\mu^{II}$, which is a computable quantity once the elastic-gravitational problem has been solved for surface and internal loads.

In minimum stress isostasy, crustal deformation is very small: $u_{nm} = h_n U_{nm}^L/g$ with $h_n = h_n^L + \zeta_n h_n^I \sim \mathcal{O}(10^{-3})$. If deflection is neglected, the topography H_{nm}^{int} of the crust-ocean boundary is given by

$$H_{nm}^{int} = \frac{\zeta_n}{x} \frac{\rho_s}{\rho_o - \rho_s} H_{nm}^{iso} \,. \tag{8}$$

This extension to finite amplitude topography introduces negligible errors in the gravitational potential (Text S6). The local shell thickness is determined from the average shell thickness d_s and the coefficients $H_{nm}^{iso} - H_{nm}^{int}$ (Eq. (S.9) in Text S5).

3.4. Bayesian Inversion

The figure of equilibrium and the isostatic model define the forward problem: given the interior structure and the isostatic load (H_{nm}^{iso}), we can predict the shape and gravity coefficients. What interests us more is the inverse problem which is nonlinear, under- or overconstrained depending on the parameter, and based on uncertain gravity and shape data. It is thus well suited to a Bayesian inference method [*Sambridge and Gallagher*,

©2016 American Geophysical Union. All Rights Reserved.

2011]. The result of the Bayesian inversion is the posterior probability density function, i.e. the conditional probability for the parameters given the data [*Tarantola*, 2005; *Gregory*, 2005]. We simulate the posterior probability density function with a Metropolis-Hastings sampler. From the generated samples, we compute for each parameter the probability density function, the mean value and the Bayesian confidence intervals (Text S4).

Enceladus and Dione are modelled as three-layer incompressible bodies made of an elastic core, an ocean, and an elastic shell. The model parameters are the densities (ρ_s, ρ_o) and thicknesses (d_s, d_o) of the ice shell and ocean (the radius r_c and density ρ_c of the core are derived parameters). The prior information is described by uniform probability density functions subjected to the constraint that the shell thickness at the south pole is not negative (Text S4 and Fig. S1). For Enceladus, the uncorrelated prior ranges are $1-60\,\mathrm{km}$ for d_s and $5-60\,\mathrm{km}$ for d_o. For Dione, the prior ranges are $1-200\,\mathrm{km}$ for d_s and $5-200\,\mathrm{km}$ for d_o. Enceladus' ocean is probably similar in composition to the ice grains in the plume ($0.5-2\%$ salt by mass [*Postberg et al.*, 2011]) while the detection of silica nanoparticles sets a 4% upper bound on the salinity [*Hsu et al.*, 2015]. The prior range for ρ_o is $1000-1040\,\mathrm{kg/m^3}$ ($0-5\%$ salt by mass) and we assume the same for Dione. Given the low pressure within the crust, the density of pure ice varies between 920 and $930\,\mathrm{kg/m^3}$ depending on the temperature, but porous ice is lighter whereas salt-rich ice is denser. For the three-layer body, the prior range for ρ_s extends from $880\,\mathrm{kg/m^3}$ (10% porosity in the upper half of the crust) to $960\,\mathrm{kg/m^3}$ (no porosity, similar salt content as the ocean maximum). For Enceladus, we model a very porous crust with a four-layer model in which the crust is made of a bottom layer with fixed density ($920\,\mathrm{kg/m^3}$) and

©2016 American Geophysical Union. All Rights Reserved.

a 10 km-thick upper layer with a prior density range of $700 - 920\,\mathrm{kg/m^3}$ [*Besserer et al.*, 2013].

4. Results

Given the compensation factor, minimum stress isostasy requires a shell nearly half as thick as in classical isostasy (Fig. 1). The compensation factor is most sensitive to the shell thickness which plays the role of compensation depth. The shear moduli of the shell and core (radius r_c) are set to $\mu_s = 3.5\,\mathrm{GPa}$ (pure ice) and $\mu_c = 40\,\mathrm{GPa}$ (hydrated silicates), respectively. The compensation factor is nearly independent of μ_s, μ_c, and r_c as long as the shell and core are not fluid-like (i.e. $\mu_s, \mu_c \gg \bar{\rho} g R = 0.05\,\mathrm{GPa}$ for Enceladus). As a simple example, we solve Eqs. (1)–(5) for the two parameters (k_2^F, f_2) and the eight hydrostatic/isostatic components of degree two, assuming zero data uncertainty and an ice-dominated mantle ($\rho_s = 925\,\mathrm{kg/m^3}$ as in *McKinnon* [2015]). For Enceladus, $(k_2^F, f_2) = (0.93, 0.36)$ and $r_c = 194\,\mathrm{km}$, while $(k_2^F, f_2) = (0.92, 0.54)$ and $r_c = 407\,\mathrm{km}$ for Dione. Fig. 1 shows that classical Airy isostasy predicts a very thin ocean for Enceladus and no ocean at all for Dione.

For Enceladus, our reference data are the coefficients (C_{20}, C_{22}, C_{30}) of the gravity solution SOL1 (Table S2), combined with the shape TOPA (Table S4). For this model, the inversion yields $d_s = 23 \pm 4\,\mathrm{km}$, $d_o = 38 \pm 4\,\mathrm{km}$, $r_c = 192 \pm 2\,\mathrm{km}$, and $\rho_c = 2422 \pm 46\,\mathrm{kg/m^3}$ at 1σ (see Fig. S1 for posterior distributions). Shell and ocean densities are not constrained. The shell and ocean thicknesses are inversely correlated (Fig. 2) because the core radius is well determined (Fig. S2). Our estimates for Enceladus' shell thickness overlap with those of librations ($21 - 26\,\mathrm{km}$ in *Thomas et al.* [2016], $14 - 26\,\mathrm{km}$ in *Van Hoolst et al.* [2016]). For a rigorous comparison, we compute the librations from the probability dis-

©2016 American Geophysical Union. All Rights Reserved.

tribution over the parameters inferred from our gravity-shape inversion assuming a rigid shell with nonhydrostatic boundaries [*Van Hoolst et al.*, 2016]. The predicted distribution (461 ± 72 m at 1σ) is wider than the distribution of observed librations (528 ± 31 m at 1σ) (Fig. 3). Thus librations put tighter bounds on the average shell thickness of Enceladus, although they do not constrain the other interior parameters.

For Dione, the inversion of shape and gravity and shape data (Tables S3 and S5) yields $d_s = 99 \pm 23$ km, $d_o = 65 \pm 30$ km, $r_c = 398 \pm 14$ km, and $\rho_c = 2435 \pm 140$ kg/m^3 (at 1σ). Errors are much larger than for Enceladus (Fig. 2) because of the large relative error on the shape (Tables S5 and S7). The gravity and shape data can thus be explained if there is a global ocean deep under the surface, whose past existence was already suggested by observation of ridge flexure [*Hammond et al.*, 2013] and thermal history models [*Multhaup and Spohn*, 2007]. We predict that Dione undergoes librations of amplitude 52 ± 10 m at 1σ (Fig. 3), one order of magnitude below Enceladus and thus not detectable in Cassini images.

5. Discussion

Comparison with librations can pinpoint data biases and constrain modelling choices. First, Enceladus' degree-three gravity favours a thinner shell than degree-two coefficients [*McKinnon*, 2015] (Fig. 1 and Table S6). Degree-two gravity however predicts a thinner shell (in agreement with librations) if C_{22} is 2σ higher than its SOL1 central value, as suggested by the alternative gravity solution SOL2 (Table S2). Alternatively, the degree-two shape could be responsible for the disagreement: while the new ellipsoidal shape of *Thomas et al.* [2016] does not affect much the results (Table S6), the recent ellipsoidal shape of *Nadezhdina et al.* [2016] predicts more degree-two compensation and thus a

©2016 American Geophysical Union. All Rights Reserved.

thinner shell. Second, we did not allow for a lot of surface porosity in our three-layer model, but we can easily do it with a four-layer model. The estimated shell thickness increases with porosity because surface topography contributes less to the gravity signal and must be less compensated (Table S6 and Fig. S3). Consistency with librations suggests however that porosity is not an important factor.

Enceladus' shell thickness varies mainly in latitude from 29 ± 4 km at the equator (zonal average) to 14 ± 4 km and 7 ± 4 km at the north and south poles, respectively (Fig. 4 and Text S5). Longitudinal variations are either subdominant, with shell thickening along the tidal axis, or could be absent altogether as suggested by the latest estimates of the ellipsoidal shape (Table S4). The very thin south polar crust facilitates the passage of water from the ocean to the surface and increases the concentration of tidal heating in the area. The variation in shell thickness could be due to crustal tidal heating which is indeed highest at the poles and lowest along the tidal axis [*Ojakangas and Stevenson*, 1989]. For Dione, shell thickness varies by less than five percent with a minimum at the poles and a maximum along the leading-trailing axis. Similarly to Enceladus, the zonal variation in shell thickness could be due to tidal heating, but we have no ready explanation for the longitudinal variation anticorrelated with tidal heating. Both satellites are more tectonized or resurfaced in their leading and trailing hemispheres than close to their tidal axis [*Crow-Willard and Pappalardo*, 2015; *Kirchoff and Schenk*, 2015].

The average crustal stress is about 30 kPa for Enceladus, which is half of the average topographic stress, as expected in isostasy [*Melosh*, 2011]. It is comparable in magnitude to tidal stresses [*Nimmo et al.*, 2007a] and could trigger the formation of the south polar terrain margins by gravitational spreading [*Yin and Pappalardo*, 2015]. We also evaluated

©2016 American Geophysical Union. All Rights Reserved.

isostatic stresses in the core in order to check that they are always smaller than isostatic stresses in the crust. Therefore, the core can be modelled as an elastic layer regarding isostatic loading. A final contentious point is that isostasy is only valid to first order in the flattening, contrary to the figure of equilibrium. The second-order error on the isostatic model, however, changes the total gravity potential [*Wieczorek and Phillips*, 1998] by less than the data uncertainty (Text S6).

Beyond Enceladus and Dione, our new take on isostasy is applicable to large icy satellites with global oceans, such as Europa [*Nimmo et al.*, 2007b], Titan [*Nimmo and Bills*, 2010], and particularly Ganymede whose gravity and shape will be measured by the JUICE mission. According to *Park et al.* [2016], gravity and shape data from the Dawn mission suggest isostasy on Ceres, but the case is far from clear because compensation does not occur for all gravity components. Finally, isostasy plays a crucial role in understanding the long-wavelength gravity and shape as well as estimating the crust thickness of the planets Mars [*Wieczorek and Zuber*, 2004], Venus [*James et al.*, 2013], and Mercury [*Perry et al.*, 2015]. Thanks to the simultaneous availability of gravity/shape and libration data, Enceladus' case constitutes the first validation of planetary-scale isostasy.

Acknowledgments. All data used here are freely available in the literature. M.B. is supported by the Brain Pioneer contract BR/314/PI/LOTIDE. A.R. is supported by the Belgian PRODEX program managed by the European Space Agency in collaboration with the Belgian Federal Science Policy Office. A.T. received support from the 'Supplementary Researcher' programme managed by the Belgian Federal Science Policy Office, and from the European Research Council (ERC) under the European Union's Horizon 2020 research and innovation programme (grant agreement No 670874).

©2016 American Geophysical Union. All Rights Reserved.

References

Besserer, J., F. Nimmo, J. H. Roberts, and R. T. Pappalardo (2013), Convection-driven compaction as a possible origin of Enceladus's long wavelength topography, *J. Geophys. Res.*, *118*, 908–915, doi:10.1002/jgre.20079.

Cadek, O., G. Tobie, T. Van Hoolst, M. Massé, G. Choblet, A. Lefèvre, G. Mitri, R.-M. Baland, M. Behounkova, O. Bourgeois, and A. Trinh (2016), Enceladus's internal ocean and ice shell constrained from Cassini gravity, shape and libration data, *Geophys. Res. Lett.*, *43*, 5653–5660, doi:10.1002/2016GL068634.

Crow-Willard, E. N., and R. T. Pappalardo (2015), Structural mapping of Enceladus and implications for formation of tectonized regions, *J. Geophys. Res.*, *120*, 928–950, doi:10.1002/2015JE004818.

Dahlen, F. A. (1981), Isostasy and the ambient state of stress in the oceanic lithosphere, *J. Geophys. Res.*, *86*, 7801–7807, doi:10.1029/JB086iB09p07801.

Dahlen, F. A. (1982), Isostatic geoid anomalies on a sphere, *J. Geophys. Res.*, *87*, 3943–3947, doi:10.1029/JB087iB05p03943.

Dahlen, F. A., and J. Tromp (1999), *Theoretical Global Seismology*, Princeton University Press.

Greff-Lefftz, M., L. Métivier, and J. Besse (2010), Dynamic mantle density heterogeneities and global geodetic observables, *Geophys. J. Int.*, *180*, 1080–1094, doi:10.1111/j.1365-246X.2009.04490.x.

Gregory, P. C. (2005), *Bayesian Logical Data Analysis for the Physical Sciences*, Cambridge University Press, Cambridge.

Hammond, N. P., C. B. Phillips, F. Nimmo, and S. A. Kattenhorn (2013), Flexure on

©2016 American Geophysical Union. All Rights Reserved.

Dione: Investigating subsurface structure and thermal history, *Icarus*, *223*, 418–422, doi:10.1016/j.icarus.2012.12.021.

Hemingway, D. J., M. Zannoni, P. Tortora, F. Nimmo, and S. W. Asmar (2016), Dione's internal structure inferred from Cassini gravity and topography, *Lunar Planet. Sci. Conf. 47, abstract 1314*.

Hsu, H.-W., F. Postberg, Y. Sekine, T. Shibuya, S. Kempf, M. Horányi, A. Juhász, N. Altobelli, K. Suzuki, Y. Masaki, T. Kuwatani, S. Tachibana, S.-I. Sirono, G. Moragas-Klostermeyer, and R. Srama (2015), Ongoing hydrothermal activities within Enceladus, *Nature*, *519*, 207–210, doi:10.1038/nature14262.

Iess, L., D. J. Stevenson, M. Parisi, D. Hemingway, R. A. Jacobson, J. I. Lunine, F. Nimmo, J. W. Armstrong, S. W. Asmar, M. Ducci, and P. Tortora (2014), The gravity field and interior structure of Enceladus, *Science*, *344*, 78–80, doi: 10.1126/science.1250551.

Jaeger, J. C., N. G. W. Cook, and R. W. Zimmerman (2007), *Fundamentals of Rock Mechanics*, 4th edition, Blackwell.

James, P. B., M. T. Zuber, and R. J. Phillips (2013), Crustal thickness and support of topography on Venus, *J. Geophys. Res.*, *118*, 859–875, doi:10.1029/2012JE004237.

Jeffreys, H. (1970), *The Earth*, Cambridge University Press, Cambridge.

Kalousová, K., O. Souček, and O. Čadek (2012), Deformation of an elastic shell with variable thickness: a comparison of different methods, *Geophys. J. Int.*, *190*, 726–744, doi:10.1111/j.1365-246X.2012.05539.x.

Kirchoff, M. R., and P. Schenk (2015), Dione's resurfacing history as determined from a global impact crater database, *Icarus*, *256*, 78–89, doi:10.1016/j.icarus.2015.04.010.

©2016 American Geophysical Union. All Rights Reserved.

Lambeck, K. (1980), Estimates of stress differences in the crust from isostatic considerations, *J. Geophys. Res.*, *85*, 6397–6402, doi:10.1029/JB085iB11p06397.

Lambeck, K. (1988), *Geophysical Geodesy*, Clarendon Press, Oxford.

McGovern, P. J., S. C. Solomon, D. E. Smith, M. T. Zuber, M. Simons, M. A. Wieczorek, R. J. Phillips, G. A. Neumann, O. Aharonson, and J. W. Head (2002), Localized gravity/topography admittance and correlation spectra on Mars: Implications for regional and global evolution, *J. Geophys. Res.*, *107*, 5136, doi:10.1029/2002JE001854.

McKinnon, W. B. (2013), The shape of Enceladus as explained by an irregular core: Implications for gravity, libration, and survival of its subsurface ocean, *J. Geophys. Res.*, *118*, 1775–1788, doi:10.1002/jgre.20122.

McKinnon, W. B. (2015), Effect of Enceladus's rapid synchronous spin on interpretation of Cassini gravity, *Geophys. Res. Lett.*, *42*, 2137–2143, doi:10.1002/2015GL063384.

Melosh, H. J. (2011), *Planetary Surface Processes*, Cambridge University Press, Cambridge.

Moritz, H. (1990), *The Figure of the Earth*, Wichmann, Karlsruhe.

Multhaup, K., and T. Spohn (2007), Stagnant lid convection in the mid-sized icy satellites of Saturn, *Icarus*, *186*, 420–435, doi:10.1016/j.icarus.2006.09.001.

Nadezhdina, I. E., A. E. Zubarev, E. S. Brusnikin, and J. Oberst (2016), A libration model for Enceladus based on geodetic control point network analysis, *Int. Arch. Photogramm. Remote Sens. Spatial Inf. Sci.*, *XLI-B4*, 459–462, doi:10.5194/isprs-archives-XLI-B4-459-2016.

Nimmo, F., and B. G. Bills (2010), Shell thickness variations and the long-wavelength topography of Titan, *Icarus*, *208*, 896–904, doi:10.1016/j.icarus.2010.02.020.

©2016 American Geophysical Union. All Rights Reserved.

Nimmo, F., J. R. Spencer, R. T. Pappalardo, and M. E. Mullen (2007a), Shear heating as the origin of the plumes and heat flux on Enceladus, *Nature*, *447*, 289–291, doi: 10.1038/nature05783.

Nimmo, F., P. C. Thomas, R. T. Pappalardo, and W. B. Moore (2007b), The global shape of Europa: Constraints on lateral shell thickness variations, *Icarus*, *191*, 183–192, doi:10.1016/j.icarus.2007.04.021.

Nimmo, F., B. G. Bills, and P. C. Thomas (2011), Geophysical implications of the long-wavelength topography of the Saturnian satellites, *J. Geophys. Res.*, *116*, E11001, doi: 10.1029/2011JE003835.

Ojakangas, G. W., and D. J. Stevenson (1989), Thermal state of an ice shell on Europa, *Icarus*, *81*, 220–241, doi:10.1016/0019-1035(89)90052-3.

Park, R. S., A. S. Konopliv, B. Bills, N. Rambaux, J. Castillo-Rogez, C. A. Raymond, A. T. Vaughan, A. Ermakov, M. T. Zuber, R. R. Fu, M. J. Toplis, C. T. Russell, A. Nathues, and F. Preusker (2016), A partially differentiated interior for (1) Ceres deduced from its gravity field and shape, *Nature*, advance online publication, doi: 10.1038/nature18955.

Perry, M. E., G. A. Neumann, R. J. Phillips, O. S. Barnouin, C. M. Ernst, D. S. Kahan, S. C. Solomon, M. T. Zuber, D. E. Smith, S. A. Hauck, S. J. Peale, J.-L. Margot, E. Mazarico, C. L. Johnson, R. W. Gaskell, J. H. Roberts, R. L. McNutt, and J. Oberst (2015), The low-degree shape of Mercury, *Geophys. Res. Lett.*, *42*, 6951–6958, doi: 10.1002/2015GL065101.

Porco, C. C., P. Helfenstein, P. C. Thomas, A. P. Ingersoll, J. Wisdom, R. West, G. Neukum, T. Denk, R. Wagner, T. Roatsch, S. Kieffer, E. Turtle, A. McEwen, T. V.

©2016 American Geophysical Union. All Rights Reserved.

Johnson, J. Rathbun, J. Veverka, D. Wilson, J. Perry, J. Spitale, A. Brahic, J. A. Burns, A. D. Del Genio, L. Dones, C. D. Murray, and S. Squyres (2006), Cassini observes the active south pole of Enceladus, *Science*, *311*, 1393–1401, doi:10.1126/science.1123013.

Postberg, F., J. Schmidt, J. Hillier, S. Kempf, and R. Srama (2011), A salt-water reservoir as the source of a compositionally stratified plume on Enceladus, *Nature*, *474*, 620–622, doi:10.1038/nature10175.

Sabadini, R., and B. Vermeersen (2004), *Global Dynamics of the Earth*, Kluwer Academic Publishers, Dordrecht.

Sambridge, M., and K. Gallagher (2011), Inverse Theory, Monte Carlo Method, in *Encyclopedia of Solid Earth Geophysics*, edited by H. K. Gupta, pp. 639–644, Springer Netherlands, Dordrecht, doi:10.1007/978-90-481-8702-7_192.

Schulson, E. M., and P. Duval (2009), *Creep and Fracture of Ice*, Cambridge University Press, Cambridge.

Tarantola, A. (2005), *Inverse Problem Theory and Methods for Model Parameter Estimation*, SIAM, Philadelphia.

Thomas, P. C., J. A. Burns, P. Helfenstein, S. Squyres, J. Veverka, C. Porco, E. P. Turtle, A. McEwen, T. Denk, B. Giese, T. Roatsch, T. V. Johnson, and R. A. Jacobson (2007), Shapes of the saturnian icy satellites and their significance, *Icarus*, *190*, 573–584, doi:10.1016/j.icarus.2007.03.012.

Thomas, P. C., R. Tajeddine, M. S. Tiscareno, J. A. Burns, J. Joseph, T. J. Loredo, P. Helfenstein, and C. Porco (2016), Enceladus's measured physical libration requires a global subsurface ocean, *Icarus*, *264*, 37–47, doi:10.1016/j.icarus.2015.08.037.

©2016 American Geophysical Union. All Rights Reserved.

Tricarico, P. (2014), Multi-layer hydrostatic equilibrium of planets and synchronous moons: Theory and application to Ceres and to solar system moons, *Astr. J.*, *782*, 99, doi:10.1088/0004-637X/782/2/99.

Turcotte, D. L., R. J. Willemann, W. F. Haxby, and J. Norberry (1981), Role of membrane stresses in the support of planetary topography, *J. Geophys. Res.*, *86*, 3951–3959, doi: 10.1029/JB086iB05p03951.

Van Hoolst, T., R.-M. Baland, and A. Trinh (2016), The diurnal libration and interior structure of Enceladus, *Icarus*, *277*, 311–318, doi:10.1016/j.icarus.2016.05.025.

Vening Meinesz, F. A. (1946), The indirect isostatic or Bowie reduction and the equilibrium figure of the Earth, *Bull. Géod.*, *1*, 33–107, doi:10.1007/BF02519025.

Wieczorek, M. A., and R. J. Phillips (1998), Potential anomalies on a sphere - Applications to the thickness of the lunar crust, *J. Geophys. Res.*, *103*, 1715–1724, doi: 10.1029/97JE03136.

Wieczorek, M. A., and M. T. Zuber (2004), Thickness of the Martian crust: Improved constraints from geoid-to-topography ratios, *J. Geophys. Res.*, *109*, E01009, doi:10.1029/2003JE002153.

Yin, A., and R. T. Pappalardo (2015), Gravitational spreading, bookshelf faulting, and tectonic evolution of the South Polar Terrain of Saturn's moon Enceladus, *Icarus*, *260*, 409–439, doi:10.1016/j.icarus.2015.07.017.

Zharkov, V. N. (2004), A theory of the equilibrium figure and gravitational field of the Galilean satellite Io: The second approximation, *Astr. Lett.*, *30*, 496–507, doi: 10.1134/1.1774402.

©2016 American Geophysical Union. All Rights Reserved.

Zharkov, V. N., and T. V. Gudkova (2010), Models, figures and gravitational moments of Jupiter's satellite Io: Effects of the second order approximation, *Planet. Space Sci.*, *58*, 1381–1390, doi:10.1016/j.pss.2010.06.004.

Zharkov, V. N., V. V. Leontjev, and V. A. Kozenko (1985), Models, figures, and gravitational moments of the Galilean satellites of Jupiter and icy satellites of Saturn, *Icarus*, *61*, 92–100, doi:10.1016/0019-1035(85)90157-5.

©2016 American Geophysical Union. All Rights Reserved.

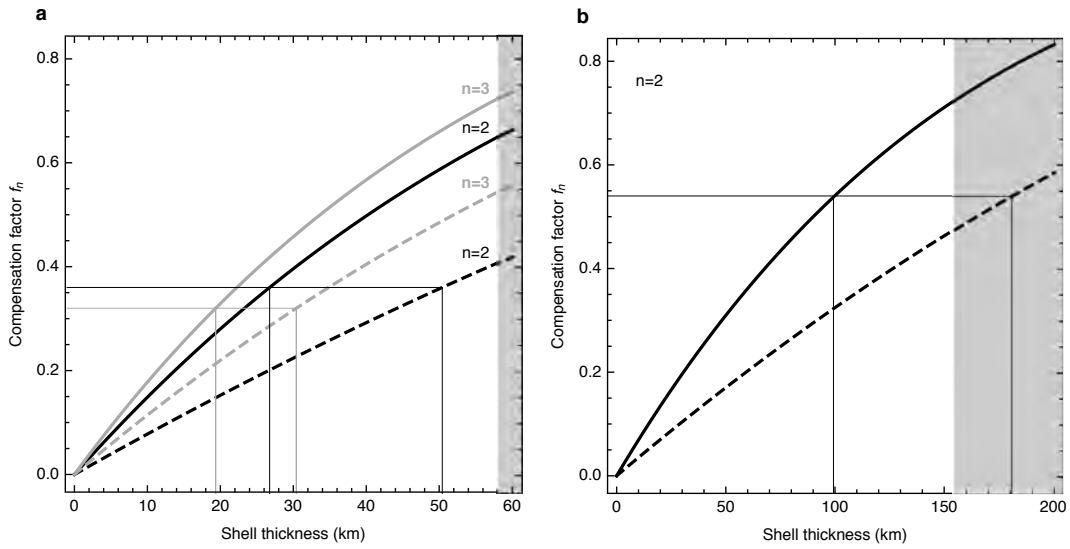

Figure 1. Compensation factor as a function of shell thickness: (a) Enceladus, (b) Dione. Minimum stress isostasy (solid curves) is computed for a three-layer model with an elastic core (radius of 194 km for Enceladus, 407 km for Dione), saline ocean (density 1020 kg/m^3), and elastic shell (density 925 kg/m^3). Classical Airy isostasy (dashed curves) is given by $f_n = 1 - (d/R)^n$. Straight lines indicate the shell thickness corresponding to (a) $f_2 = 0.36$, $f_3 = 0.32$ and (b) $f_2 = 0.54$. Shaded areas indicate crust-core overlap.

©2016 American Geophysical Union. All Rights Reserved.

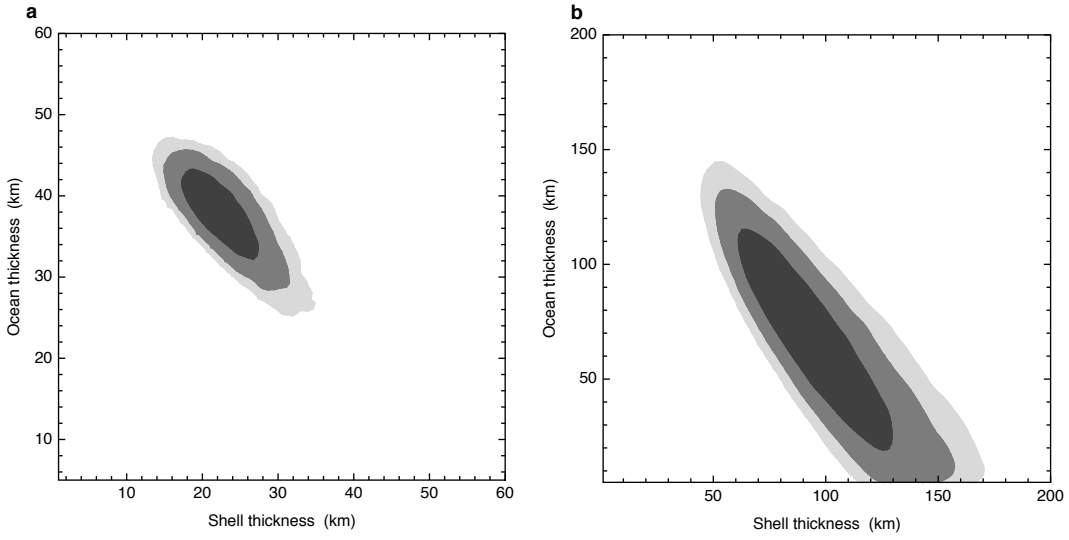

Figure 2. Inferred shell and ocean thicknesses: (a) Enceladus, (b) Dione. Contours show Bayesian confidence regions to $(1\sigma, 2\sigma, 3\sigma)$. The ranges on the axes correspond to the prior uniform distributions. The inverse correlation between shell and ocean thicknesses is clearly visible.

©2016 American Geophysical Union. All Rights Reserved.

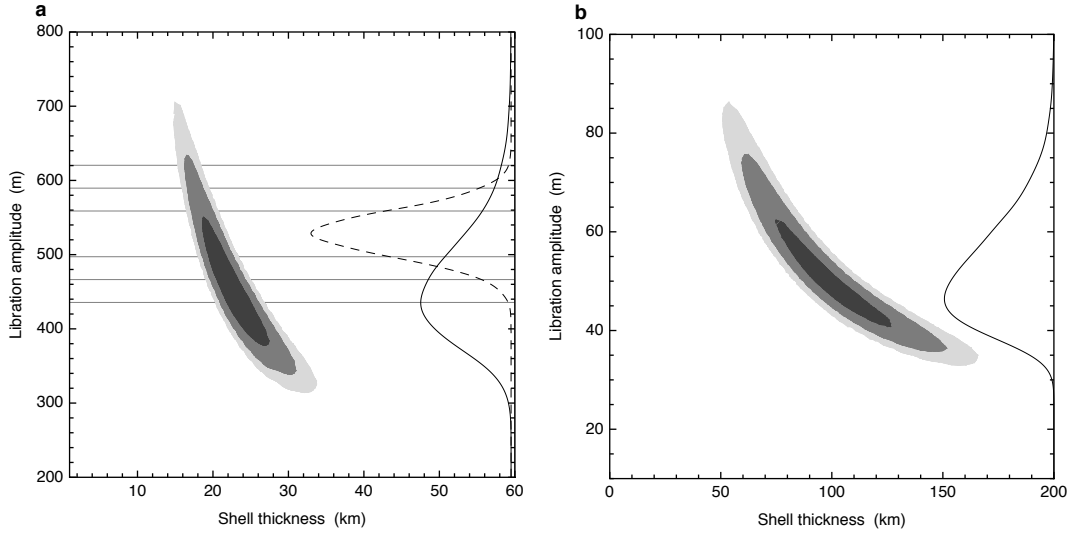

Figure 3. Libration amplitude: (a) Enceladus, (b) Dione. Contours show Bayesian confidence regions for models resulting from the gravity-shape inversion ($1\sigma, 2\sigma, 3\sigma$). Solid curves show the distributions of inferred librations. In panel (a), the dashed curve shows the distribution of observed librations [*Thomas et al.*, 2016] with horizontal lines indicating the ($1\sigma, 2\sigma, 3\sigma$) ranges.

©2016 American Geophysical Union. All Rights Reserved.

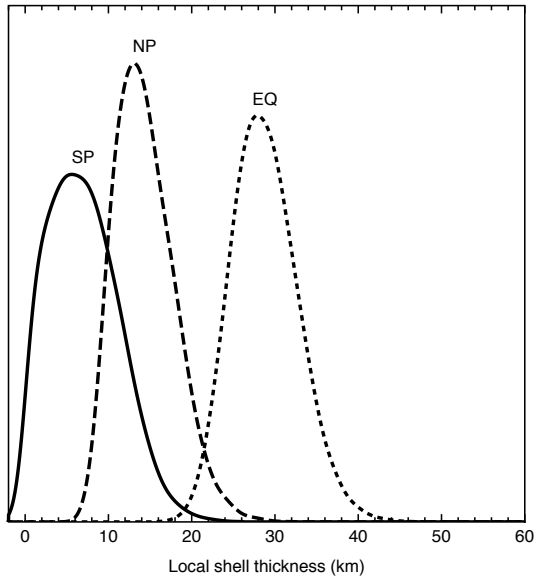

Figure 4. Local shell thickness of Enceladus. Solid, dashed, and dotted curves show the distributions of the inferred shell thickness at the south pole (SP), north pole (NP) and equator (EQ), respectively. The equatorial thickness represents the zonal average. Negative values are an artefact of histogram smoothing.

©2016 American Geophysical Union. All Rights Reserved.